Superexchange-mediated negative thermal expansion in Nd-doped $BiFeO_3$

Christopher M. Kavanagh, Philip Lightfoot and Finlay D. Morrison*

School of Chemistry and EaStCHEM, University of St Andrews, St Andrews, KY16 9ST, United Kingdom

Abstract

A detailed powder neutron diffraction study of $Bi_{0.7}Nd_{0.3}FeO_3$ shows it is a G_z-type antiferromagnet adopting the space group *Pn´ma´*. Detailed structural analysis using both Rietveld and symmetry mode analysis indicates that competition between geometric effects and magnetic superexchange results in unusual evolution of octahedral tilting and structural distortion on cooling. These changes are manifested in both the electrical response which displays relaxor-type behaviour and also in a region of negative thermal expansion below 200 K.

Introduction

$BiFeO_3$ is a widely studied multiferroic due to its ferroelectric (high $T_C \sim 1083 – 1103$ K) and (anti)ferromagnetic properties ($T_N \sim 643$ K) which may be utilised in device applications.[1] However, $BiFeO_3$ has a rich and complex chemistry and various studies have highlighted the influence on synthetic route and conditions on formation of single phase $BiFeO_3$ and its thermodynamic stability[2-6]. For applications the utilisation of $BiFeO_3$ is further hindered by electrical conductivity due to non-stoichiometry[7]; several studies have shown that appropriate doping on either A- or B-cation sites can reduce unwanted leakage currents. One of the most common doping strategies is replacement of the Bi by a rare earth cation; for example substitution of the volatile Bi^{3+} with rare earths *e.g.* Nd^{3+} ($Bi_{1-x}Nd_xFeO_3$) can improve the electrical properties and thermal stability of the perovskite phase[8, 9]. Many authors have sought to use such A-site substitution to manipulate the crystal structure and stabilise a second, intermediate, polar polymorph and hence introduce a morphotropic phase boundary (MPB) to enhance the functional properties. (However, it is important to note that in many cases authors misuse the term ‘MPB’ to describe the Curie transition between the polar (*R3c*-$BiFeO_3$) phase

and the non-polar, paraelectric '$GdFeO_3$' phase adopted by rare earth-rich compositions). A recent review by Arnold[10] gives a succinct summary of many of the systems studied. The $Bi_{1-x}Nd_xFeO_3$ system has been studied in some detail and a phase diagram proposed based on conventional solid-state synthesis[11-14]; this is of particular interest as an intermediate antipolar phase has been reported[13, 14]. The following phase sequence is proposed at room temperature: *R3c* ($0 < x \leq 0.125$) $\Leftrightarrow$ '*Pbam*' ($0.125 < x \leq 0.25$) $\Leftrightarrow$ *Pbnm* ($x > 0.25$). More specifically, the intermediate '*Pbam*' phase has a $PbZrO_3$-like antipolar superlattice, with a $\sqrt{2}\ a_p$ x $2\sqrt{2}\ a_p$ x 4 a_p unit cell, relative to the aristotype cubic perovskite (a_p). The final, paraelectric *Pbnm* phase has the common $GdFeO_3$-like structure, with a $\sqrt{2}\ a_p$ x $\sqrt{2}\ a_p$ x 2 a_p unit cell. This structure is also adopted by the parent end member $NdFeO_3$ ($x = 1$) which is a G-type antiferromagnetic with a Néel temperature of 690 K.[15-17]). Neutron and X-ray diffraction studies of Sosnowska *et al*.[18, 19] have highlighted a number of interesting magnetic interactions - they report a C-type antiferromagnetic ordering of Nd^{3+} moments at very low temperatures *circa*. < 1.5 K.[19] More importantly, the Fe-Fe interactions order creating a cell that conforms to a G_z-type antiferromagnetic cell above 200 K.[19] (Note that the results of Sosnowska were reported using the *Pbnm* setting and for the following discussion those results have been transcribed to the conventional *Pnma* setting for comparison with the results presented in this work). Below 200 K, there is a coherent rotation of the FeO_6 octahedra and a spin reorientation in the *b-c* plane resulting in an additional component, G_y, to the magnetic cell.[19] This is due to the increase in the Fe-O2-Fe angle associated with the in-phase tilt and an increase of the axial Fe-O1 bond lengths without changes of the Fe-O1-Fe angles associated with the anti-phase tilt.[19] This spin reorientation transition has been observed between 100 – 190 K where the Fe^{3+} magnetic moments gradually change direction.[19] The corresponding rotation of the octahedra may affect the electrical properties, as it will change the freedom of the A-site cations to displace causing a change in polarisability. An A-site displacement has been reported in $NdFeO_3$, which occurs in the *a-c* plane of the *Pnma* cell (*Pbnm*: *a-b* plane). There is also a very slight negative thermal expansion (NTE) in the *a* lattice parameter below 160 K, the other axes display 'normal' positive thermal expansion and overall $NdFeO_3$ displays positive volumetric expansion at all temperatures.[18, 19]

Returning to the $Bi_{1-x}Nd_xFeO_3$ system it is important to note that although $x = 0.30$ adopts the paraelectric *Pnma* symmetry at room temperature the phase boundary as a function of temperature is poorly defined, specifically whether this composition enters the *Pbam* phase on cooling to sub-ambient. In the absence of variable temperature crystallographic data many

authors use physical property (*e.g.* dielectric) measurements to infer structural changes. However in the $Bi_{1-x}La_xFeO_3$ system (with $x = 0.5$) we had noted that a peak in permittivity need not be associated with a crystallographic (symmetry changing) phase transition[20].

Here we report a variable temperature powder neutron diffraction (PND) study on $Bi_{1-x}Nd_xFeO_3$ where x = 0.3 and demonstrate that non-polar *Pnma* symmetry is preserved at all temperatures. However, symmetry mode analysis has been used to highlight more unusual and subtle structural effects on cooling; these distortions result from a delicate balance of geometric (steric) effects and magnetic ordering. These result in a significant change in the electrical behaviour. In addition, the material exhibits a significant region of negative thermal expansion (NTE) behaviour with a net volume expansion of the unit cell of *ca.* 0.1%.

Experimental Methods

The synthesis was performed *via* conventional solid-state methods. Stoichiometric amounts of Bi_2O_3 and Fe_2O_3 were mixed with Nd_2O_3 (due to its highly hygroscopic nature the latter was dried at 1000 °C prior to weighing). The mixed powders were ball milled in ethanol using a Fritsch Pulverisette 7 planetary micro ball mill (600rpm, 1 hr.). The dry powder was pelletized in a uniaxial press using a 13mm stainless steel die; a pressure of ca. 70 MPa was applied to the pellet. The powders were then calcined in a two-step reaction. In the initial step, pelleted samples were heated to 800 °C for 5hrs. The powder was re-milled under the same conditions and pelleted before sintering at 1000 °C for a further 5 hrs. Resulting pellets were *ca.* 91% of theoretical density with a uniform grain size 5-10 μm (see ESI figure S1).

Silver paste electrodes were applied to the pellet faces and cured at 120 °C prior to electrical characterisation. Both isothermal *ac* immittance spectroscopy and capacitance and loss "sweep" measurements were carried out between 50 and 750 K. Sub-ambient measurements were carried out in a Sumitomo HC-2 closed-cycle He cryogenics system; above-ambient measurements were carried out by placing the sample in a bespoke sample holder in a Carbolite tube furnace. Electrical data was collected using a combination of Hewlett Packard 4192A LF and Agilent 4294A impedance analysers. All data were corrected for sample geometry.

Powder neutron diffraction (PND) experiments were performed on the HRPD diffractometer at the ISIS neutron spallation source using a closed cycle refrigerator. Rietveld refinements were carried out using the general structural analysis system (GSAS) and its associated

graphical user interface program (EXPGUI).[21, 22] Only data from the backscattering detector bank ($2\theta \approx 168°$) on the HRPD instrument were used for refinements ($0.7 < d < 2.6$ Å).

Results

A. Rietveld Refinements - Preliminary structural analysis

The variable temperature PND data were analysed using the Rietveld method. The preliminary analysis shows $Bi_{1-x}Nd_xFeO_3$ where x = 0.30 (hereafter BNFO30) is predominantly a $GdFeO_3$-like phase (space group *Pnma)*. Isotropic atomic displacement parameters were used for all atoms. Although samples appeared to be single phase perovskite by laboratory PXRD analysis, a trace amount of Fe_2O_3 secondary phase (*circa*. 1 wt%) was detected in the PND data, which remains constant in all refinements. Figure 1 shows the Rietveld refinement profile of BNFO30 at 300 K with the corresponding unit cell parameters and atom positions shown in Table 1.

The *Pnma* structural model was further refined with a G_z-type antiferromagnetic model of the magnetic structure, described with Shubnikov symmetry as *Pn′ma′*. This is the equivalent cell to the parent G_x-type magnetic cell of $NdFeO_3$ refined in the *Pbnm* setting.[18, 19] The net magnetic moment was determined from refinements with the moment fixed solely along the *c*-axis (which gave the most stable refinements as discussed in more detail below). The net magnetisation, Figure 2, ranges from *ca*. 4.2 μ_B at 50 K to 3.2 μ_B at 500 K; these values are comparable to the (room temperature) moments of 4.00 μ_B and 3.87 μ_B reported for $BiFeO_3$[23] and $NdFeO_3$[19], respectively. Fitting of the net magnetisation to a power law, Equation 1, assuming a mean field approximation, gave a Néel temperature, T_N of 642 +/- 84 K with an exponent, α, of 0.25 +/- 0.06. The extrapolation, however, is over a significant range and the error is therefore large. Conventional magnetisation measurements were not possible due to the presence of small amounts of ferromagnetic Fe_2O_3.

$$F(T) \propto (T_N - T)^{\alpha} \qquad \text{Equation 1}$$

Numerous studies show that orthoferrites can have off-axis magnetic components.[19, 24] These additional components would influence the diffraction pattern, so we carefully checked for these possibilities. Attempts at refining an off-axis magnetic moment produced unstable models with near zero magnetic moments. Simulations of the powder diffraction pattern using the software ISODISTORT[25] show that the *Pn′ma′* model with a magnetic component along

the *a*-axis adds intensity uniquely on magnetic reflections at (*hkl*) = (012), (030), and a structural and magnetic reflection at (210). At 100 K, these reflections should occur at 2.58 Å, 2.61 Å, and 2.63 Å d-spacing, respectively, the latter two points being outside the range of the backscattering detectors. There is no sign of additional magnetic intensity in the 90° bank data and in the backscattering bank no intensity at 2.58 Å is distinguishable. An off-axis component along the *a*-axis is therefore precluded. There are no easily distinguished unique reflections for a magnetic component along the *b*-axis. Other magnetic models were tested at low temperature to eliminate the possibility of spin reorientation, however, the G_z-type magnetic cell with the moment fixed along the *c*-axis remained the best refinement. The goodness-of-fit parameters, χ^2, wR_p, and R_p for the other magnetic models are given in the Electronic Supplementary Information, ESI (Table S1), along with example refinements showing the magnetic contributions to the PND data and G_z magnetic cell.

Although this analysis shows that the chosen structural and magnetic models are unambiguous there is some evidence of anisotropic peak broadening below 200 K. This was modelled with a Lorentzian function (GSAS profile function 3, which is designed to model macroscopic strain). The profile adds six additional empirical terms which were systematically evaluated. Analysis showed that the L_{11} (γ_{11}) and L_{33} (γ_{33}) terms have the most significant impact on the quality of the fit by broadening (*h*,*l*)-dominated reflections. With inclusion of these terms the refinement profile and corresponding agreement factors of models with and without anisotropic peak broadening at 50 K (see ESI Figures S1 and S2 and Table S2) demonstrates a significant improvement to the quality of the fit.

The temperature dependent PND study (50 - 500 K) revealed the evolution of the unit cell parameters, as shown in Figure 3. On cooling, all three axes and the unit cell volume show typical contraction over a wide temperature range until around 200 K. Between 200 K and 50 K there is a similar contraction in the *a*-axis and concomitant expansion of the *c*-axis. Over the same range, there is also negative thermal expansion in the *b*-axis. This negative thermal expansion (NTE) in the *b*- and *c*-axes results in an overall NTE of the unit cell volume as a function of increasing temperature (Figure 3). This is rather unusual; for example in the related $Bi_{0.5}La_{0.5}FeO_3$ phase, magnetostriction results in an "invar" effect where the volume becomes invariant at low temperature.[20]

The volumetric expansion coefficient, α_v, in each temperature regime ($50 < T < 180$ K and $200 < T < 500$ K) were estimated using Equation 2:

$$\alpha_v(T) = \frac{1}{V_0} \cdot \frac{\delta V}{\delta T} \qquad \text{Equation 2}$$

The calculated average thermal expansion coefficient is 2.18×10^{-5} K^{-1} for the expansion of the unit cell above 200 K (and varies between 3.48×10^{-5} and 5.18×10^{-6} K^{-1}). In the NTE region (50 K to 180 K) the average α_v is -7.59×10^{-6} K^{-1} (and ranges from -1.32×10^{-5} K^{-1} to -2.05×10^{-6} K^{-1}). The result is a volumetric expansion of *ca*. 0.14% on cooling from 180 to 50K. This change in expansion is clearly significant and can be explained with changes in the physical properties of the material *i.e.*, magnetism and bonding, as outlined in the following sections.

B. Immittance data

The electrical properties of a ceramic material are closely related to the microstructure and the homogeneity of a ceramic. Typically, a polycrystalline ceramic material is comprised of different electroactive regions e.g., grain boundary and bulk, which can be described by the brickwork model.[26,27] The model describes the regions in terms of an equivalent circuit; placing the regions in a series combination described with a resistive (*R*) and capacitive (*C*) element representing the various charge transfer and polarisation processes, respectively.

The electroactive regions typically have different magnitudes of associated *R* and *C*. This allows techniques such as ac immittance spectroscopy to separate the different electrical responses in the frequency domain as each region has a different time constant, τ.

$$\tau = RC = \frac{1}{2\pi f_{max}} \qquad \text{Equation 3}$$

Where $f_{\max}$ is the corresponding relaxation frequency in Hz. Each RC element has a corresponding semi-circular arc in the complex impedance (Z^*) and electric modulus (M^*) plane plot with the diameter of the arc proportional to the resistance and inverse capacitance, respectively. The individual RC elements also give rise to Debye-like peaks in the spectroscopic plots of the imaginary component (Z'' or M'' vs. frequency); the frequency at which the peak maximum, f_{max}, occurs is determined by the time constant (Equation 3).

Although the magnitude of the resistance can vary dramatically depending on a number of factors, there are typical magnitudes of capacitance associated with each type of electroactive region (as determined by relative permittivity and geometry).[28] Assignments of the electroactive responses are based on the magnitude of associated capacitance of the regions *i.e.*, typical magnitudes of capacitance for a grain boundary response are of the order 10^{-10}–10^{-8} Fcm^{-1} compared to typical bulk values of 1×10^{-12} to 1×10^{-11} Fcm^{-1}.[27]

In this study, a combined approach was undertaken to study the electrical properties using immittance spectroscopy and fixed frequency capacitance and loss measurements over a temperature range 50 – 300 K. Immittance spectroscopy shows the electrical response of the BNFO30 sample has at least two electroactive regions, which are clearly visible in the electrical modulus (Figure 4) and impedance (ESI, Figure S5).

Typically, the dominant feature in the electrical modulus is associated with the bulk response due to the relative magnitude of the bulk capacitive response to that of the grain boundary. To confirm the origin of features in the immittance spectra the permittivity of the electroactive responses can be determined from either from the diameter of the semi-circular arc in the complex electric modulus, which scales directly as $1/\varepsilon_r$, or from the M'' peak (Figure 4b) where the peak magnitude also scales inversely with permittivity (and therefore capacitance) according to:

$$M''_{max} = \frac{1}{2\varepsilon_r} = \frac{\varepsilon_0}{2C} \qquad \text{Equation 4}$$

By estimating the magnitude of semi-circular arcs in the complex modulus, it was possible to determine the capacitive response of each electroactive region (*i.e. RC* element). At 280 K, for example, the capacitance (*C*) associated with the component that dominates the complex modulus is 13.3 pFcm^{-1}. Based on the magnitude of capacitance this was assigned as the bulk response.[27]

Reviewing the M'' spectra on cooling shows the Debye-like M'' peak associated with the bulk decreases in magnitude and moves to lower frequency (Figure 4b). The diminishing peak height represents an increase in the capacitance of the bulk whereas the displacement of the peak to lower frequencies indicates the resistance of the sample increases as shown by Equation 3. The Debye-like peak leaves the measureable frequency window *ca.* 174 K. Below this temperature the bulk response can be tracked with fixed frequency total capacitance measurements as justified below.

Fixed frequency, total capacitance (C_p) and loss ($tan\ \delta$) measurements, performed on the BNFO30 sample allowed for the analysis of the capacitive behaviour at temperatures below those where individual relaxations could be observed. Assuming an equivalent circuit of two parallel *RC* elements in series (representing the bulk and grain boundary regions *i.e.*, the bricklayer model), the parallel capacitance (C_p) as a function of frequency results in a high

frequency plateau.[28] This plateau contains contributions from both bulk (C_b) and grain boundary (C_{gb}) capacitances according to:

$$C_P = \left(C_{gb}^{-1} + C_b^{-1}\right)^{-1} \qquad \text{Equation 5}$$

The magnitudes of the capacitive responses in the BNFO30 pellet are such that C_{gb}>>C_b. This means that the overall contribution of the grain boundary to the total capacitance at high frequency is small and C_p is effectively that of the bulk response. Bulk capacitance data extracted from M^* at higher temperatures can be used to validate this assumption (C_{gb}>>C_b) from which the relative permittivity of the bulk were calculated based on:

$$C_P = \varepsilon_r \varepsilon_0 \frac{A}{d} \qquad \text{Equation 6}$$

For simplicity, the total effective permittivity at 1 MHz has been plotted as a function of temperature (Figure 5) and there is good agreement between the effective permittivity based on the total capacitance and bulk permittivity values as determined from M^* plots. The relative permittivity ranges from *circa*. 110 – 210 and peaking around *circa*. 160 K. At higher temperature, there is a dramatic upturn in the 1 MHz data due to an increasing contribution from the grain boundary/electrode response. Although there is no phase transition in the crystallographic sense (*i.e*. change in space group) this broad feature in the permittivity data occurs in the same temperature range as the change in the lattice parameter behaviour (Figure 3) and so is linked to some local change the crystal structure and in the polarisation dynamics. It is important to note that due to the sub-ambient temperatures studied here, the measured permittivity response below *ca*. 200 K is free from significant influence of long range conduction and grain boundary/electrode polarisation effects which typically plague such measurements of related systems at higher temperature.

Plotting the relative permittivity and loss at multiple frequencies shows a frequency dependence which is characteristic of relaxor-type behaviour (as shown by the frequency dispersion and displacement in the peak maxima, Figure 6). The frequency dependence in the peak maxima means that the peak position varies by *ca*. 20 °C between 1 kHz and 1 MHz. This frequency dependence reflects a distribution of local environments which can occur due to inhomogeneity on a nanometre scale. In BNFO30, this is probably due to A-site disorder with regional clusters of neodymium and bismuth. It has been suggested clusters of nano-regions may be interacting at low temperature,[29, 30] creating a spectrum of relaxation times, which

correspond to random local relaxation processes. The frequency dispersion in the relative permittivity can be typically be analysed with a Vogel-Fulcher (VF) expression, Equation 7:

$$f = f_0 e^{-E_a/k(T_m - T_f)} \qquad \text{Equation 7}$$

where f corresponds to the frequency of applied field, f_0 is the limiting response frequency of the local (dipolar) polarisation process, E_a is the associated activation energy, k is the Boltzmann constant, T_m is the temperature at which the relative permittivity is at its maximum for a given frequency (f) and T_f is the static (dipole) freezing temperature.

Based on Equation 7, fitting the dielectric data to this function (Figure 7) allows the freezing temperature (T_f) to be determined. An unrestricted (free) fit of this function results in an unrealistic fundamental response frequency of the dipoles, f_0 = 1.057x10^{17} Hz, and a dipole freezing temperature, T_f, of 83 K. Typically dipole response frequencies range between 10^9 - 10^{12} Hz. Using these as limits for f_0 results in the freezing temperature values ranging from *ca.* 110 to 126 K (see ESI Table S3).

As pointed out by Rotaru *et al.*,[31, 32] parameters obtained from fitting of data to the Vogel Fulcher are highly variable and sensitive to the selection of data for the fit (*e.g.* the frequency rnage used, the effect of noise at low frequency, and inductive effects at high frequency); this is due to the large extrapolation required to obtain T_f and f_0 from the low and high frequency asymptotic limits, respectively. This sensitivity and high degree of variability is demonstrated by the need to fix f_0 to a realistic response frequency as described above: VF analysis can lead to unreliable and unrealistic physical parameters due to fitting the curvature of T_m over a narrow frequency range and the subsequent extrapolation to determine T_f. Consequently, methods that are more robust can be used to give frequency independent parameters such as the analysis of the dielectric loss, ε'', with Jonscher's universal dielectric response (UDR) model. UDR describes the frequency dependent response of the ε'' by:[33]

$$\varepsilon'' = \frac{1}{(f/f_p)^{-m} + (f/f_p)^{1-n}} \qquad \text{Equation 8}$$

where f is the applied frequency, f_p is the frequency at which the ε'' reaches a maxima and exponent terms describe the gradient of the response below (m) and above (1-n) the peak frequency, respectively (Figure 7b). The two exponents m and n allow for the fitting of asymmetric peaks found in relaxors and has allowed values between $0 \leq m,n \leq 1$. For a perfect Debye response, the gradient before and after the peak maxima in a *log* ε'' vs. *log* f (Hz) plot should be +1 and -1 respectively *i.e.*, $m = 1$, and $n = 0$.

As expected with relaxor-type behaviour, the ε'' peak of the bulk response in the BNFO30 sample shows significant broadening, as seen in the plot of *log* ε'' vs. *log f* (Hz) (Figure 7b). Critically, we observe that the gradient of the electroactive response, *m*, shown in Figure 7b decreases on cooling. This is due to the sample approaching a critical freezing temperature, T_f, below which the dipoles will have a frequency-independent response, meaning the gradient, *m*, should tend towards zero when approaching the freezing temperature.

The minor secondary component which is present in the high temperature data means that the gradient *m* shown in Figure 7c as a function of temperature, had to be carefully determined for a series of temperatures. The deviation at low temperature is associated with a gradual change in the quality of the fit in *m* as the gradient is determined close to the peak maxima. Therefore, an extrapolation over the linear part of the curve from 110 – 136 K was performed avoiding potential additional contributions at temperature extremes. On cooling, the gradient, *m*, of the ε'' response tends toward zero as the freezing temperature is approached, Figure 7b; therefore extrapolating to $m = 0$ results in an estimated freezing temperature, T_f, of 96 K +/- 3 K. This is close to that of the VF analysis where the analysis showed that the freezing temperature lies within a range 110 - 126 K.

Bulk conductivities, σ_b (= R_b^{-1}) were estimated over a range of temperature using capacitances obtained from M^* and $M''_{\max}$ frequency using the relationship $RC = 1/2\pi f_{max}$, equation 3. The conductivity determined from M^* data show the expected temperature dependence described by the Arrhenius expression:

$$\sigma_b = \sigma_0 e^{-\frac{E_a}{kT}} \qquad \text{Equation 9}$$

The bulk activation energy (E_a) was determined to be ~0.35 eV which is consistent with other experimental studies[34] and is characteristic of electronic conduction dominated by polaron hopping[35] (see ESI, Figure S6, for Arrhenius plot).

C. Correlation between structural behaviour and dielectric/magnetic response

Changes in the magnitude of the relative permittivity of the bulk response are typically associated with structural changes that can be monitored by diffraction data. Therefore, we now discuss correlations between structural changes determined from the Rietveld refinement of PND data and the electrical characterisation. The structural analysis uses a combination of

conventional 'bond length/bond angle' analysis and symmetry-mode analysis using the online structural analysis tool ISODISTORT.[25]

The $GdFeO_3$-type structure with space group *Pnma* is the most commonly adopted by perovskite oxides and is described by the $a^-b^+a^-$ tilt system (or $a^-a^-c^+$ in the alternate *Pbnm* setting). Typically this tilting is commonly explained by cation size effects whereby an under-sized A-cation relative to that of the B-site and oxygen lattice results in a Goldschmidt tolerance factor (t) less than 1[36,37]; the BO_6 octahedra tilt and the A-cations displace to reduce the volume of the A-site coordination environment. In a more detailed treatment Woodward describes the effects on the tilt system as an attempt to maximise the A-O covalent bonding while minimising the repulsive A-O overlap.[38] To minimise the A-O repulsive interactions and maximise the covalent bonding as a function of temperature (instead of composition) the octahedra must rotate. The expectation is that on cooling the distortion (and tilting) should increase.

The evolution of these distortions can be monitored by conventional analysis of diffraction data or, alternatively, using ISODISTORT symmetry-mode analysis. ISODISTORT represents the distortion from the ideal cubic perovskite structure in terms of symmetry-specific distortion modes rather than changes in individual atomic positions, and consequent changes in the observed angles and bond lengths. Examples of its use in related systems, $LaFeO_3$ and $Bi_{0.5}La_{0.5}FeO_3$, have been given recently[20, 39].

Conventional Rietveld refinements showed that all Fe-O bond lengths contract on cooling as expected, Figure 8 (see also Figure 9 for naming of O-atoms). However, the contraction is not completely linear over the studied temperature range. The rate of contraction in the axial Fe-O1 bond, shown in Figure 8, deviates markedly below *circa*. 180 K; this is close to the maximum in the relative permittivity measured at 1 MHz, Figure 5. Similarly, the longest Fe-O bond length (Fe-O2) shows compression in a similar temperature range.

These changes in the Fe-O bond lengths also have corresponding changes with the O-Fe-O *intra*-octahedral bond angles (Figure 8b). On cooling from *circa*. 200 K, 4 of the pairs of O-Fe-O angles deviate away from 90° and the remaining 2 pairs of *circa*. 90° angles between the axial and equatorial plane tend towards 90°; thus the octahedra become less distorted. The 4 paired angles are linked to the R_5^+ [O] distortion mode which describes the axial oxygen atoms undergoing a slightly different displacement than that of the equatorial plane with respect to the R_4^+ tilt mode (discussed in more detail below).

Evaluation of the *inter*-octahedral Fe-O-Fe angles shows both the Fe-O1-Fe and Fe-O2-Fe angles show an unexpected *increase* upon cooling below 200 K (Figure 8c). The Fe-O-Fe angles increase at different rates, resulting in the *inter*-octahedral angles becoming most equivalent around 180 K. The Fe-O-Fe bond angles are comprised of contributions from both the tilt system and distortion modes of the octahedra.

ISODISTORT represents the anti-phase and in-phase tilts in terms of the R_4^+ and M_3^+ modes, respectively. The magnitude of the tilt modes decrease anomalously on cooling below 200 K, Figure 10a, corresponding to the increases in Fe-O-Fe angles, Figure 8c. Above 200 K, the tilt modes are almost invariant, 'plateauing' prior to the 'expected' decrease at higher temperatures (typically, systems will tend towards higher (un-tilted) symmetry at higher temperature).

In this case, a significant contribution to the unusual thermal evolution of Fe-O-Fe bond angles comes from the in-phase tilt around the *b*-axis and anti-phase tilt around the *a*-axis. On cooling below 200 K, the Fe-O1-Fe angle (Figure 8c) tends towards 180°. This is due to a decreasing R_4^+ octahedral tilt mode, which means the *b*-axis will expand on cooling (Figure 3). This expansion is offset slightly by the change in the axial Fe-O1 bond length (Figure 8a).

To demonstrate the relation between the R_4^+ (anti-phase) octahedral tilt and the *b*-axis, a graphical representation of the anti-phase tilt is shown in Figure 9. The Fe-O bonds are depicted in order to highlight the Fe-O-Fe angles. If the octahedra are considered to be rigid (*i.e.*, equivalent Fe-O bond lengths), upon cooling, the increasing Fe-O-Fe angle (shown by the green solid line) would result in the pseudo cubic unit cell length *b* (yellow dashed line) and *b*-axis expanding. The expansion along *b* is due to the decreasing tilt having a larger effect than the expected contraction in the Fe-O1 bond length (Figure 8) and therefore the unit cell expands on cooling.

The Fe-O2-Fe angle increases due to the M_3^+ (in-phase) tilt, which has a similar effect on the unit cell as the anti-phase tilt. The effect on the lattice of the decreasing in-phase tilt mode is a uniform expansion in the *ac* plane. On cooling below 200 K, the Fe-O2-Fe angle increases which means the pseudo cubic cell length expands and the cell lengths *a* and *c* should uniformly expand. The unusual thermal response of both the *b* and *c* axes are therefore directly correlated with the anomalous trends in octahedral tilting. The contraction in the *a*-axis on cooling (Figure 3), which is the more conventional behaviour, depends on a more subtle interplay of octahedral tilting and bond length contraction. Although the increasing M_3^+ tilt on cooling must lead to a contributory expansion of the *a*-axis, the R_4^+ tilt has no direct effect on the *a*-axis (the tilt is

around this axis, and so affects *c* but not *a*). The contrasting behaviours of the *a* and *c* axes are therefore explained: *both* tilts affect the *c*-axis in the same sense, but only the weaker effect of the M_3^+ tilt affects *a*, and the resulting expansion caused by this is insufficient to override the Fe-O bond length contraction.

As described by Woodward[38], the octahedral tilts and A-site displacements are intimately linked and so the latter were also considered. The A-site displacements are represented by the R_5^+ [A-site] and X_5^+ [A-site] modes and indicate displacement along *c* and *a*, respectively. The R_5^+ [A-site] and X_5^+ [A-site] track with the orthorhombic strain (D_o) shown in Figure 10b and 10c. The orthorhombic distortion parameter, D_o, represents the strain in the structure and is defined in Equation 10, where *a* and *c* are the unit cell lengths:

$$\boldsymbol{D_o} = \frac{2|\boldsymbol{a} - \boldsymbol{c}|}{(\boldsymbol{a} + \boldsymbol{c})} \qquad \text{Equation 10}$$

Over the temperature range 50 to 200 K the change in the magnitude of the X_5^+ [A-site], the displacement along *a*, is larger than that of the R_5^+ [A-site] (Table 2). However, the X_5^+ displacement decreases with decreasing temperature, which correlates with the contraction along *a*, as is observed in Figure 3. The relative contributions of the various modes can be considered by comparing their relative change in magnitude, δ, over this temperature range where:

$$\delta = |mode_{200\,K}| - |mode_{50\,K}| \qquad \text{Equation 11}$$

In addition to the magnitude of distortion, the sign of the parameter δ denotes increasing (negative δ) and decreasing (positive δ) distortion from the cubic aristotype. From the δ values presented in Table 2 it is clear that the R_5^+ [A-site] displacement along *c* is not only the largest, but it is the only mode to tend away from the ideal cubic aristotype on cooling below 200 K *i.e.*, δ is negative. Note that δ for the R_5^+ [O] mode is also negative, but this mode is also unique in that it changes sign between 200 and 50 K (Figure 10d). The latter mode corresponds to the "scissoring" distortion where the axial (O1) oxygens change from being under-rotated (negative R_5^+ [O]) relative to the equatorial Fe-O2 plane at 200 K to over-rotated (positive R_5^+ [O]) at 50 K.

The A-site displacements in response to the octahedral tilting can be understood when considering the A-O interatomic distances (ESI, Figure S7). As the M_3^+ mode decreases on cooling, the rotation of the octahedra will affect the A-site displacements directionally in the *ac* plane. The rotation means that, in general, the A-O1 interatomic distances will increase on

cooling if the octahedron is pointing towards the A-site - the converse is also true. This means that the shortest A-O1 bond lengths expand and the longest A-O1 distances contract on cooling. For the axial oxygens, the A-O2 distances will expand if the corresponding Fe-O-Fe angle points towards the A-site. Again, the converse is true. Given the distribution of the longest A-O interatomic distances, the Bi^{3+} lone pair is probably directed along the *c*-axis in an alternating antiparallel fashion.

A trial refinement with anisotropic A-site temperature factors shows that the U_{33} increases below 200 K with a proportional decrease in the U_{22} parameter (see ESI Figure S8). This might suggest a shift in the direction of the thermal vibrational mode (atomic displacements) associated with the A-site from the *b*–axis to the *c*-axis. However, the magnitudes of U_{ij} are very small. The disordered Nd and Bi cations at the A-site are likely to behave differently due to the steric effect of the Bi lone pair and it is important to emphasise, of course, that the diffraction data and subsequent analysis provides an averaged A-site effect.

In summary, subtle structural changes have been highlighted in relation to the relative permittivity. The origin of the structural distortions is presumably a competition between a purely structural geometry (bonding) optimisation and magnetostrictive effects arising from the antiferromagnetic ordering. The effect of magnetism as a driving force for structural variations is discussed in terms of superexchange. The ideal conditions for superexchange to occur are when the Fe-O-Fe bond angles are at 180°, resulting in optimal orbital overlap. On cooling, the net magnetisation in BNFO30 increases (Figure 2) and the Fe-O-Fe angles tend toward 180° (Figure 8c); accordingly, both the in-phase, M_3^+, and anti-phase tilts, R_4^+, decrease in magnitude (Figure 9). This is highly unusual: in the absence of magnetic influences, such as in $CaTiO_3$, the M_3^+ and R_4^+ tilts are expected to increase on cooling[40]. Indeed, this behaviour is also observed in AFM $LaFeO_3$[39]. Moreover, we note that the observation of NTE is very unusual in conventional (i.e. three-dimensionally-connected) perovskites, whereas it is more commonly observed in layered perovskites[41]. Recent theoretical work has suggested that the possibility for NTE in layered system is enhanced due to higher elastic anisotropy; conversely NTE driven by purely structural (rather than magnetostrictive) effects is predicted to be rare in 3-D perovskites.[42]

Considering purely structural effects, driven by the optimisation of chemical bonding, the expectation is that the tilting modes and A-site displacement modes should all increase on cooling; this is evidently not the case. Therefore magnetism, and A-cation displacement behaviour must also play a role. In principle, AFM superexchange favours a less distorted

crystal structure with 180° overlap of the *p-d* hybridised orbitals, and hence drives a reduction in tilting on cooling. This unusual magnetostrictive effect also manifests itself to a lesser extent in the A-site displacement being compromised.

The most significant factor with respect to the optimisation of bond lengths is likely to be optimisation of bonding at the A-site. This should tend to displace the A-site atom further from the centre of its coordination environment as the temperature decreases (in the absence of magnetic influences). This is the case in most non-magnetic perovskites, e.g. $CaTiO_3$, where both R_5^+ and X_5^+ modes increase in absolute magnitude on cooling.[40]

Conclusions

A combination of electrical and structural analysis using variable temperature PND has shown that Nd-doped $BiFeO_3$ (composition $Bi_{0.7}Nd_{0.3}FeO_3$) is a semiconducting ($E_a \sim 0.35$ eV) relaxor-type material which adopts the $GdFeO_3$ structure (space group *Pnma*) with G_z-type antiferromagnetism. The observation of negative thermal expansion within the system prompted further investigation into the crystallographic changes driving this unusual thermal evolution. The detailed crystallographic changes (structural distortions) were analysed using both conventional Rietveld analysis and the symmetry mode tool ISODISTORT. The analysis shows that the structural and dielectric behaviour is influenced by superexchange, which drives anomalous changes in the tilt behaviour of the FeO_6 octahedra at low temperature. These changes occur well below the Néel temperature (642 K) due to a competition between chemical bonding and the G_z-type antiferromagnetic order. Superexchange favours linear Fe-O-Fe interactions, which means the in-phase, M_3^+, and anti-phase, R_4^+, tilts *decrease* on cooling rather than increasing, as would be expected in the absence of magnetostrictive effects. This results in more subtle effects, such as octahedral distortions and an anomalous shortening of the axial Fe-O1 bond, together with correspondingly compromised A-site displacements. These structural changes give rise to a corresponding change in the permittivity. The A-site displacements in the *ac* plane (R_5^+ and X_5^+ modes) correlate with the orthorhombic strain and are in competition with the tilt modes. In particular, the X_5^+ (A-site) mode *decreases* anomalously on cooling. The contrasting thermal evolution of the unit cell, *viz*. contraction along the *a*-axis, versus expansion of the *b*- and *c*-axes (and unit cell volume) at low temperature can clearly be ascribed to a distinctive 'un-tilting' phenomenon, which is driven

by the conflicting tendencies to optimise the magnetic superexchange interactions and the bonding requirements of the two different A-site cations.

Acknowledgements

We thank the Science and Technology Facilities Council for access to the ISIS neutron facility (RB1210111). CMK would like to thank the EPSRC for provision of a studentship *via* the doctoral training grant (EP/K503162/1). The research data supporting this publication can be accessed at DOI: 10.17630/cfd84657-908f-42c9-aad7-fb70b8583188.

References

1. G. Catalan and J. F. Scott, *Advanced Materials*, 2009, **21**, 2463-2485.
2. M. Valant, A. K. Axelsson and N. Alford, *Chemistry of Materials*, 2007, **19**, 5431-5436.
3. S. M. Selbach, M. A. Einarsrud and T. Grande, *Chemistry of Materials*, 2009, **21**, 169-173.
4. M. S. Bernardo, T. Jardiel, M. Peiteado, A. C. Caballero and M. Villegas, *Journal of the European Ceramic Society*, 2011, **31**, 3047-3053.
5. T. Rojac, A. Bencan, B. Malic, G. Tutuncu, J. L. Jones, J. E. Daniels and D. Damjanovic, *Journal of the American Ceramic Society*, 2014, **97**, 1993-2011.
6. J. Walker, P. Bryant, V. Kurusingal, C. Sorrell, D. Kuscer, G. Drazic, A. Bencan, V. Nagarajan and T. Rojac, *Acta Materialia*, 2015, **83**, 149-159.
7. W. Eerenstein, F. D. Morrison, J. Dho, M. G. Blamire, J. F. Scott and N. D. Mathur, *Science*, 2005, **307**, 1203; author reply 1203.
8. J. Walker, B. Budic, P. Bryant, V. Kurusingal, C. C. Sorrell, A. Bencan, T. Rojac and N. Valanoor, *IEEE Trans Ultrason Ferroelectr Freq Control*, 2015, **62**, 83-87.
9. D. Kan, L. Palova, V. Anbusathaiah, C. J. Cheng, S. Fujino, V. Nagarajan, K. M. Rabe and I. Takeuchi, *Advanced Functional Materials*, 2010, **20**, 1108-1115.
10. D. C. Arnold, *IEEE Trans Ultrason Ferroelectr Freq Control*, 2015, **62**, 62-82.
11. I. Levin, M. C. Tucker, H. Wu, V. Provenzano, C. L. Dennis, S. Karimi, T. Comyn, T. Stevenson, R. I. Smith and I. M. Reaney, *Chemistry of Materials*, 2011, **23**, 2166-2175.
12. I. Levin, S. Karimi, V. Provenzano, C. L. Dennis, H. Wu, T. P. Comyn, T. J. Stevenson, R. I. Smith and I. M. Reaney, *Physical Review B*, 2010, **81**, 020103.
13. S. Karimi, I. M. Reaney, Y. Han, J. Pokorny and I. Sterianou, *Journal of Materials Science*, 2009, **44**, 5102-5112.
14. S. Karimi, I. M. Reaney, I. Levin and I. Sterianou, *Applied Physics Letters*, 2009, **94**, 112903.
15. R. L. White, *Journal of Applied Physics*, 1969, **40**, 1061-1069.
16. D. Treves, *Journal of Applied Physics*, 1965, **36**, 1033-1039.
17. S. C. Parida, S. Dash, Z. Singh, R. Prasad, K. T. Jacob and V. Venugopal, *Journal of Solid State Chemistry*, 2002, **164**, 34-41.
18. R. Przeniosło, I. Sosnowska, M. Loewenhaupt and A. Taylor, *Journal of Magnetism and Magnetic Materials*, 1995, **140-144**, 2151-2152.

19. W. Sławiński, R. Przeniosło, I. Sosnowska and E. Suard, *Journal of Physics: Condensed Matter*, 2005, **17**, 4605.
20. C. M. Kavanagh, R. J. Goff, A. Daoud-Aladine, P. Lightfoot and F. D. Morrison, *Chemistry of Materials*, 2012, **24**, 4563-4571.
21. A. C. Larson and R. B. Von Dreele, *General Structure Analysis System (GSAS) Los Alamos National Laboratory Report LAUR 86-748*, Los Alamos National Laboratory 1994.
22. B. H. Toby, *Journal of Applied Crystallography*, 2001, **34**, 210-213.
23. P. Fischer, M. Polomska, I. Sosnowska and M. Szymanski, *Journal of Physics C: Solid State Physics*, 1980, **13**, 1931-1940.
24. T. Peterlin-Neumaier and E. Steichele, *Journal of Magnetism and Magnetic Materials*, 1986, **59**, 351-356.
25. B. J. Campbell, H. T. Stokes, D. E. Tanner and D. M. Hatch, *Journal of Applied Crystallography*, 2006, **39**, 607-614.
26. N. J. Kidner, N. H. Perry, T. O. Mason and E. J. Garboczi, *Journal of the American Ceramic Society*, 2008, **91**, 1733-1746.
27. J. T. S. Irvine, D. C. Sinclair and A. R. West, *Advanced Materials*, 1990, **2**, 132-138.
28. A. R. West, D. C. Sinclair and N. Hirose, *Journal of Electroceramics*, 1997, **1**, 65-71.
29. D. Viehland, S. J. Jang, L. E. Cross and M. Wuttig, *Journal of Applied Physics*, 1990, **68**, 2916-2921.
30. K. Hirota, S. Wakimoto and D. E. Cox, *Journal of the Physical Society of Japan*, 2006, **75**, 111006.
31. A. Rotaru, D. C. Arnold, A. Daoud-Aladine and F. D. Morrison, *Physical Review B*, 2011, **83**, 184302.
32. A. Rotaru and F. D. Morrison, *Journal of Thermal Analysis and Calorimetry*, 2015, **120**, 1249-1259.
33. A. K. Jonscher, *Dielectric Relaxation in Solids*, Chelsea Dielectrics Press, London, 1983.
34. K. Kalantari, I. Sterianou, S. Karimi, M. C. Ferrarelli, S. Miao, D. C. Sinclair and I. M. Reaney, *Advanced Functional Materials*, 2011, **21**, 3737-3743.
35. M. S. Islam, *Journal of Materials Chemistry*, 2000, **10**, 1027-1038.
36. V. M. Goldschmidt, *Naturwissenschaften*, 1926, **14**, 477.
37. C. A. Randall, A. S. Bhalla, T. R. Shrout and L. E. Cross, *Journal of Materials Research*, 1990, **5**, 829-834.
38. P. M. Woodward, *Acta Crystallographica Section B Structural Science*, 1997, **53**, 44-66.
39. C. A. L. Dixon, C. M. Kavanagh, K. S. Knight, W. Kockelmann, F. D. Morrison and P. Lightfoot, *Journal of Solid State Chemistry*, 2015, **230**, 337-342.
40. K. S. Knight, *Journal of Alloys and Compounds*, 2011, **509**, 6337-6345.
41. K. J. Cordrey, M. Stanczyk, C. A. Dixon, K. S. Knight, J. Gardner, F. D. Morrison and P. Lightfoot, *Dalton Trans*, 2015, **44**, 10673-10680.
42. C. Ablitt, S. Craddock, M. S. Senn, A. A. Mostofi and N. C. Bristowe, *Npj Computational Materials*, 2017, **3**.

Table 1: Atomic coordinates of the $Bi_{0.7}Nd_{0.3}FeO_3$ *Pn'ma'* phase refined from the 300 K PND data; a = 5.61889(4) Å, b = 7.81949(5) Å, c = 5.45226(4) Å.

Site	***x***	***y***	***z***	U_{iso} **(Å^2)**
Bi/Nd	0.04671(15)	0.25	0.9933(2)	0.0063(2)
Fe	0	0	0.5	-0.00058(16)
O1	0.4750(3)	0.25	0.0883(3)	0.00536(18)
O2	0.20193(18)	0.54305(13)	0.19982(18)	0.00536(18)

Table 2: The seven distortion modes (Å), based on PND refinements at 50 and 200 K.

Temperature (K)	**R_4^+ [O]**	**R_5^+ [A-site]**	**R_5^+ [O]**	**X_5^+ [A-site]**	**X_5^+ [O]**	**M_2^+ [O]**	**M_3^+ [O]**
200	1.361	-0.075	-0.023	0.521	0.274	0.022	1.087
50	1.336	-0.092	0.035	0.489	0.250	0.012	1.021
δ (Å)*	0.025	-0.017	-0.058	0.0324	0.024	0.010	0.066

*δ denotes the change in magnitude of each distortion mode between 200 and 50 K (see main text, Equation 11).

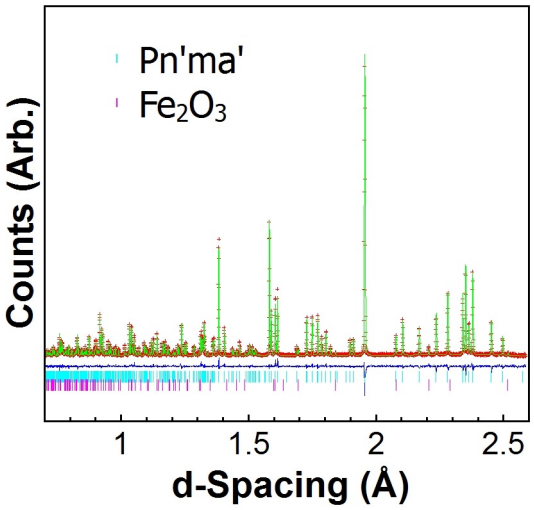

Figure 1: Rietveld refinement profile (isotropic model) of the 300 K PND data; $\chi^2 = 2.574$, $wR_p = 0.0500$ $R_p = 0.0467$ Tick marks represent Bragg reflections for *Pn'ma'* phase (top) and Fe_2O_3 (bottom).

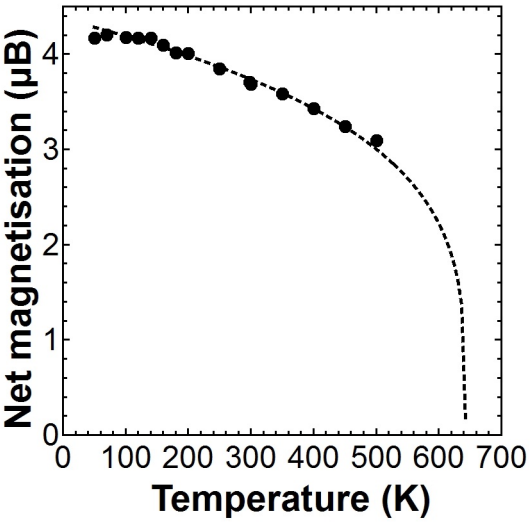

Figure 2: Net magnetisation along the *c*-axis as a function of temperature in $Bi_{0.7}Nd_{0.3}FeO_3$ derived from the Rietveld refinement. The dotted line represents a mean-field fit of the magnetic data to a power law.

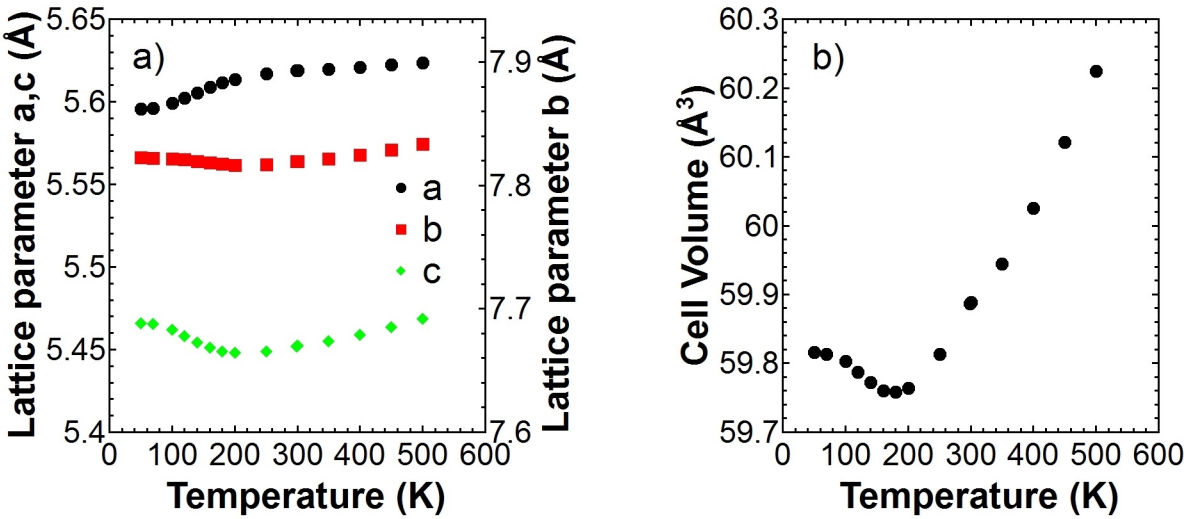

Figure 3: a) Lattice parameters and b) reduced unit cell volume as a function of temperature.

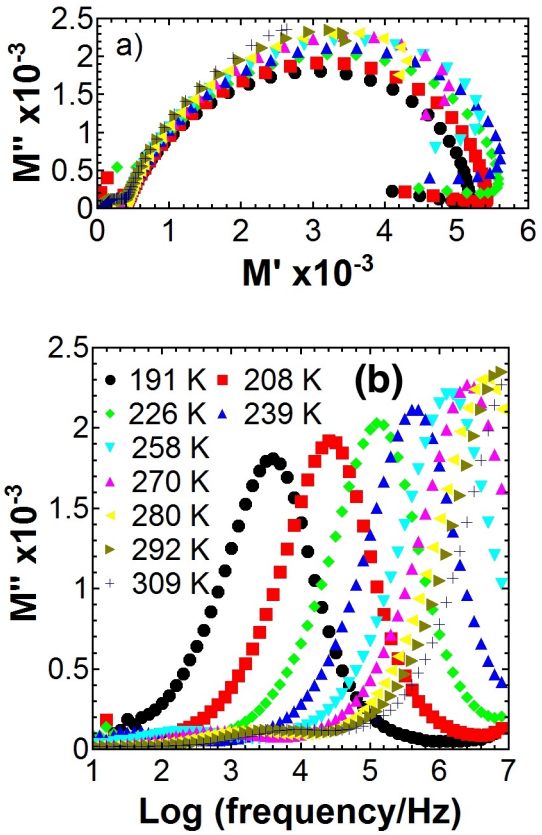

Figure 4: a) Complex modulus, M^*, as a function of temperature showing two electroactive components. b) M'' spectra show the electroactive response of the bulk dominating the electrical response. (Symbols in part (a) are as in (b).)

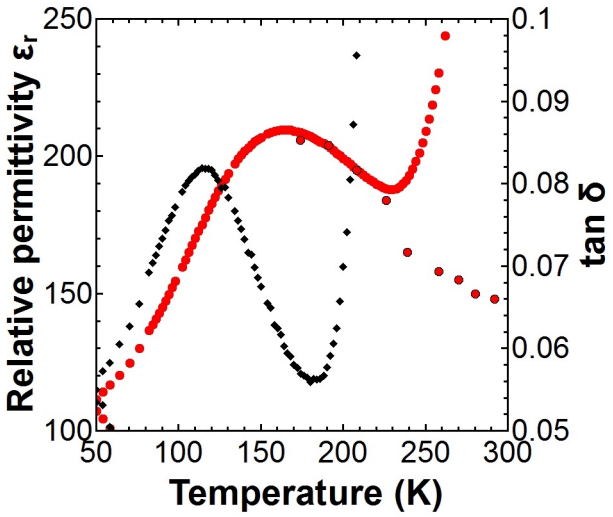

Figure 5: Relative permittivity (circles) and tan δ (diamonds) is shown as a function of temperature (1 MHz). Bulk permittivity values determined from modulus data obtained from isothermal measurements are included (circles with black outline).

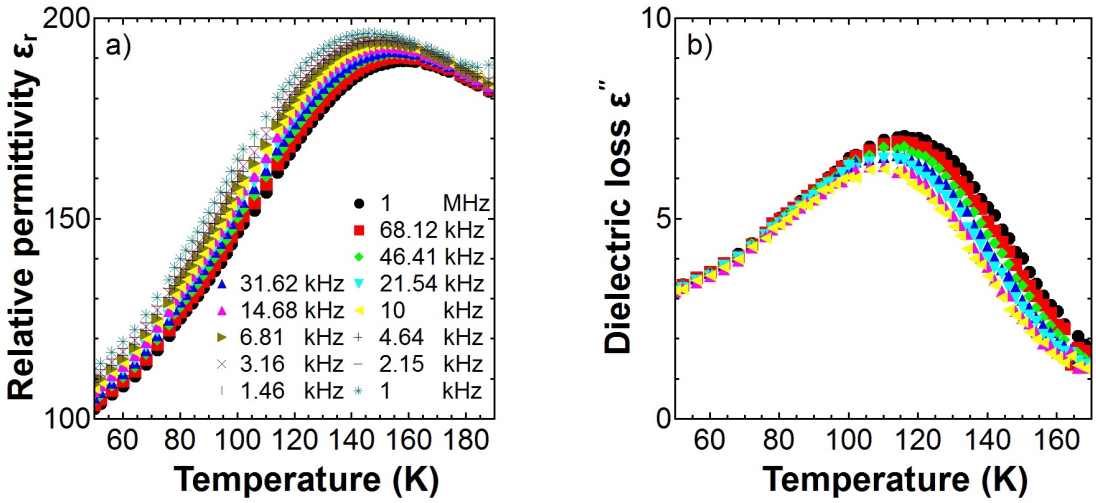

Figure 6: Plot of the relative permittivity (a) and dielectric loss (b) as a function of temperature showing a frequency dispersion at low temperature. Symbols in part (a) and (b) are the same

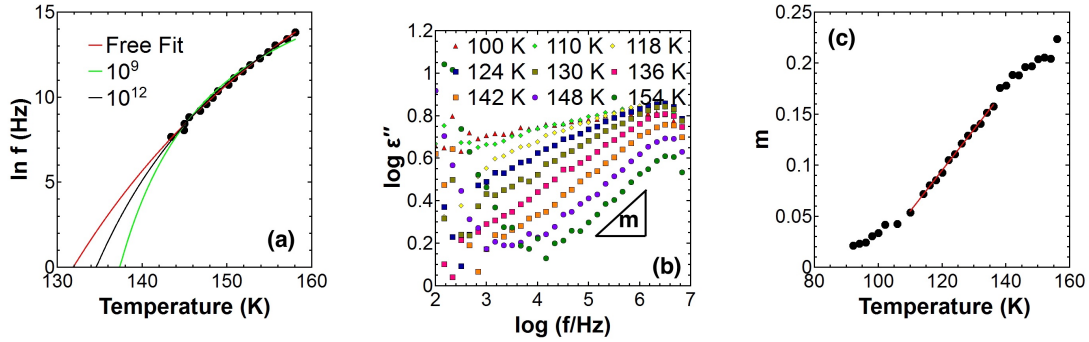

Figure 7: a) Vogel-Fulcher fits of ln *f vs*. T_m data showing a "free" fit (red) and fits where limits for the dipole response frequency f_0 (green and black) have been applied. b) Dielectric loss spectra (*log ε″* vs. *log f*) at selected temperatures. c) Gradient, *m*, of the response shown in the *log ε″ vs*. *log f* plot as a function of temperature.

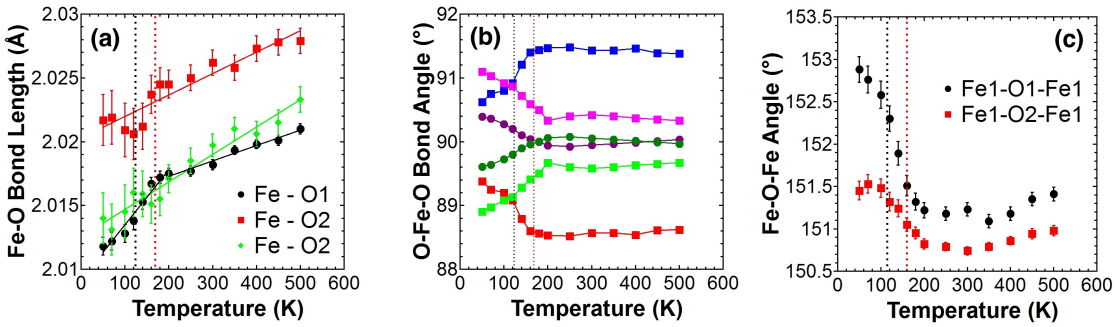

Figure 8: a) Fe-O bond lengths, showing a change in the Fe-O bond lengths around 160 K, b) axial-to-equatorial O1-Fe-O2 (squares) and the equatorial-to-equatorial O2-Fe-O2 (circles) bond angles and c) Fe-O-Fe angles as a function of temperature, which increases, on cooling. (For reference, black and red dotted lines indicate temperatures corresponding to maxima in *tan δ* and *ε ′*, respectively, at 1 MHz).

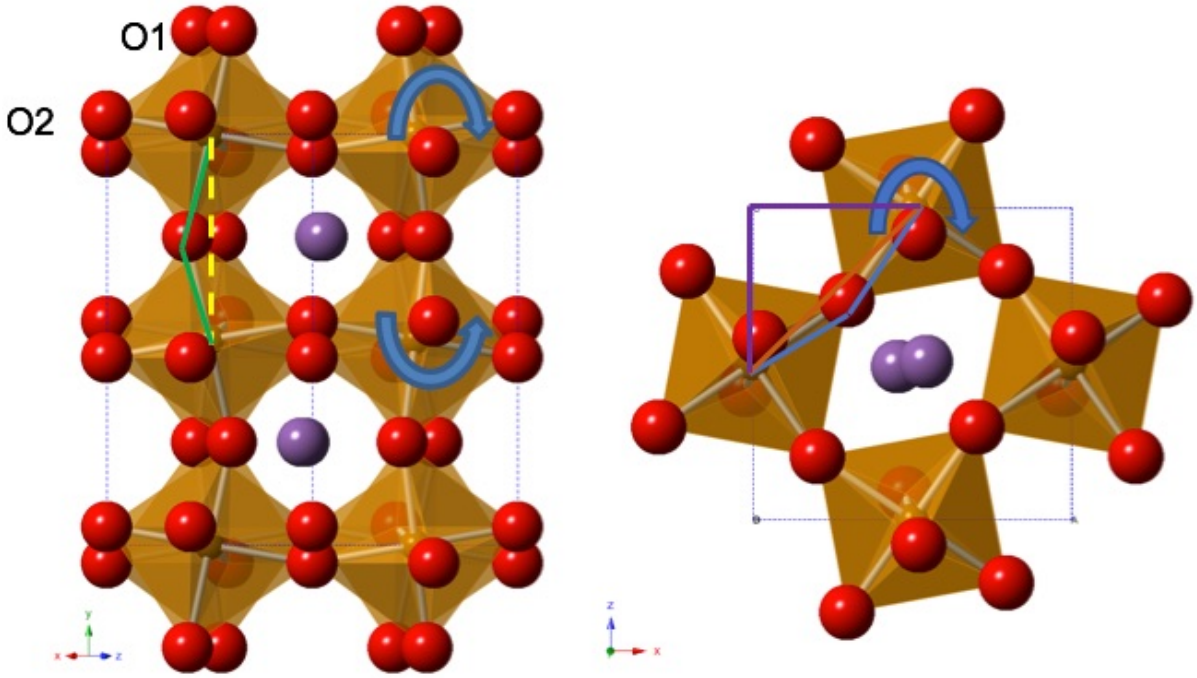

Figure 9: Anti-phase, R_4^+, rotation in the (101) plane (left) and the in-phase, M_3^+, rotation about the *b*-axis, (right).

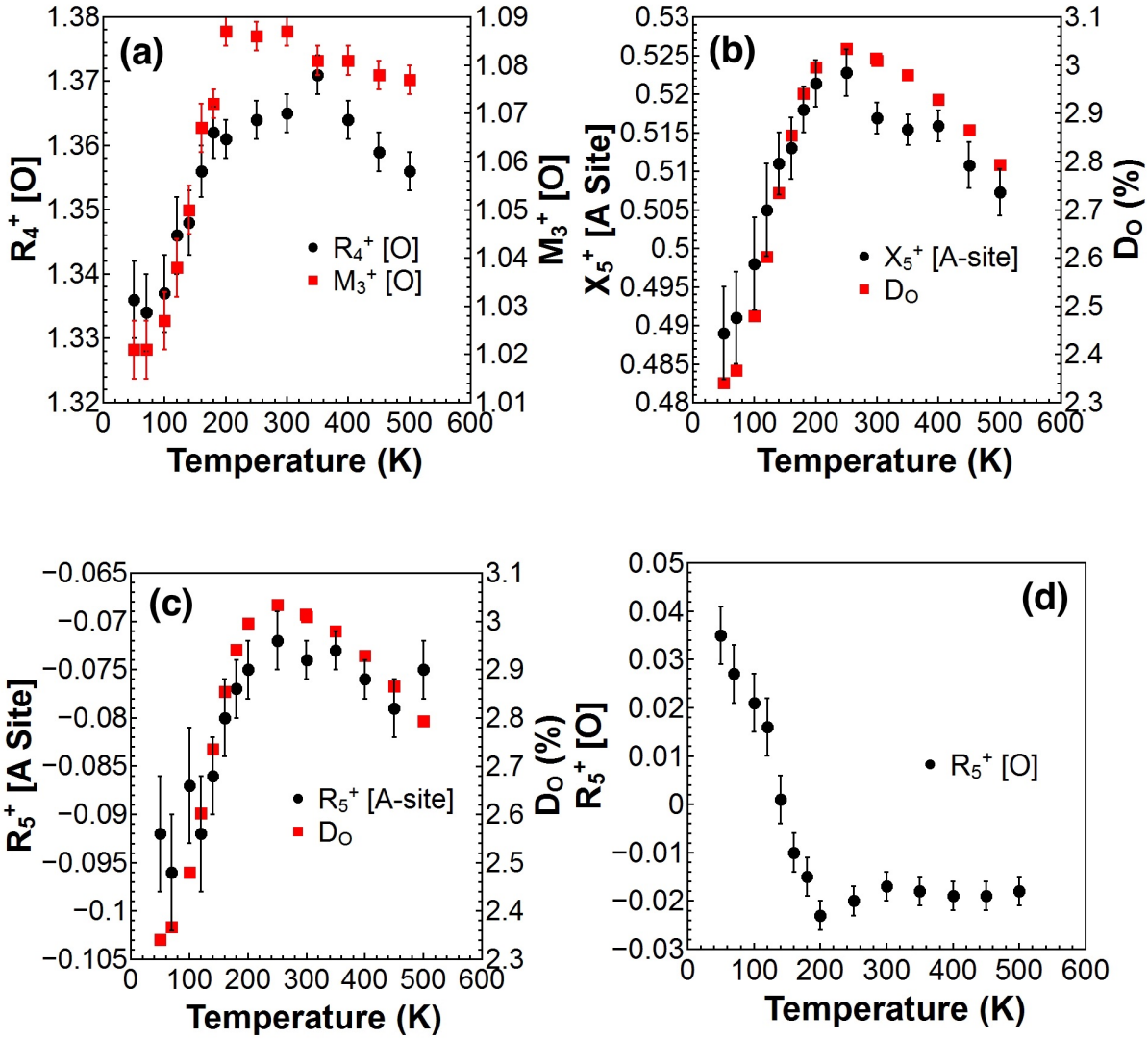

Figure 10: a) M_3^+ mode showing the in-phase rotation about *b*-axis and R_4^+ mode showing the anti-phase tilt, b) X_5^+ and c) R_5^+ [A-site] modes representing a displacement along *a* and *c* respectively. The distortion modes correlate with the degree of the orthorhombic distortion. d) R_5^+ [O] mode corresponding to the scissoring distortion where the axial oxygens (O1) are allowed to move along *c* while the equatorial oxygens (O2) displace along *b*.

Superexchange-mediated negative thermal expansion in Nd-doped $BiFeO_3$

Christopher M. Kavanagh, Philip Lightfoot and Finlay D. Morrison*

School of Chemistry and EaStCHEM, University of St Andrews, St Andrews, KY16 9ST, United Kingdom

Electronic Supplementary Information

Table S1: Goodness-of-fit parameters for magnetic and non-magnetic refinements of the *Pnma* model at 100 K.

Magnetic Symmetry	**Space group**	χ^2	wR_p	R_p
G_z	*Pn'ma'*	9.552	0.0971	0.0802
G_y	*Pn'm'a*	11.810	0.1080	0.0962
G_x	*Pnma*	11.860	0.1820	0.0947
(non-magnetic)	*Pnma*	13.090	0.1137	0.1047

Table S2: Goodness-of-fit parameters for refinements with and without L_{xx} strain terms.

Model	**Spacegroup**	χ^2	wR_p	R_p
No strain terms	*Pn'ma'*	8.647	0.0925	0.0763
Profile 3 L_{33}	*Pn'ma'*	5.19	0.0717	0.0626
Profile 3 L_{33} L11	*Pn'ma'*	4.898	0.0696	0.0624
Profile 3 L_{xx} (6 terms)	*Pn'ma'*	3.522	0.059	0.0536

Table S3: The freezing temperatures and associated errors for are shown for fixed values of f_0 as obtained from Vogel-Fulcher fits of permittivity data.

f_0 **(Hz)**	**ln** f_0	T_f**(K)**	E_a**(eV)**	χ^2	R^2
10^9	20.7	126.1 ± 0.7	0.02 ± 0.01	5.88×10^{-2}	0.985
10^{12}	27.6	110.7 ± 0.7	0.057 ± 0.001	1.76×10^{-2}	0.996

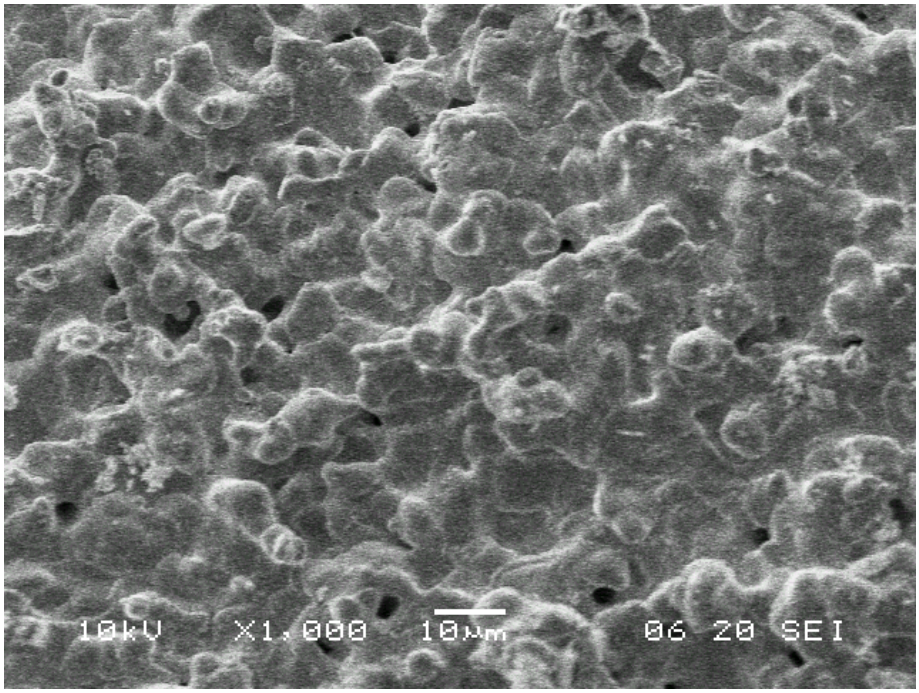

Figure S1: Scanning electron micrograph of $Bi_{0.7}Nd_{0.3}FeO_3$ pellets sintered at 1000 °C.

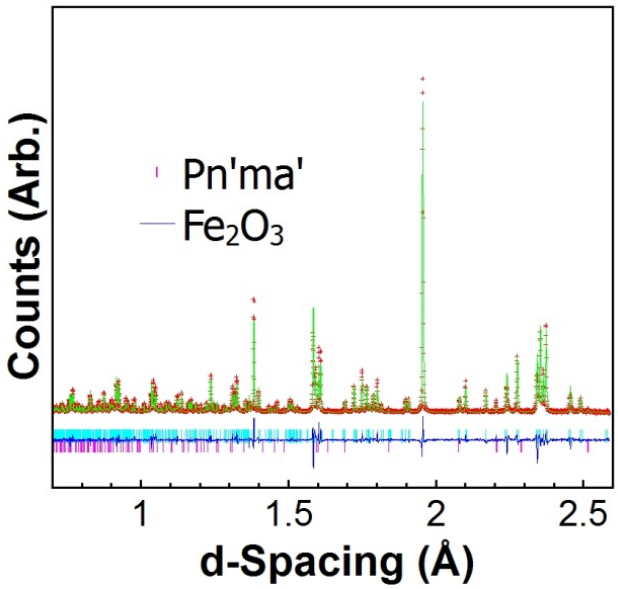

Figure S2: Isotropic refinement of the 50 K PND data showing a poor quality of fit due to the modelling of peak shapes; $\chi^2 = 8.647$, $wRp = 0.0925$, $Rp = 0.0763$.

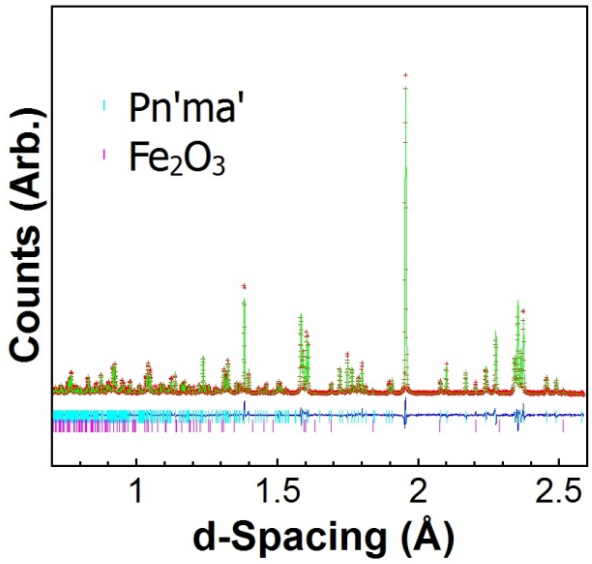

Figure S3: Refinement profile of the 50 K data with anisotropic L_{33} and L_{11} peak broadening terms; $\chi^2 = 4.898$, $wR_p = 0.0696$ $R_p = 0.0624$.

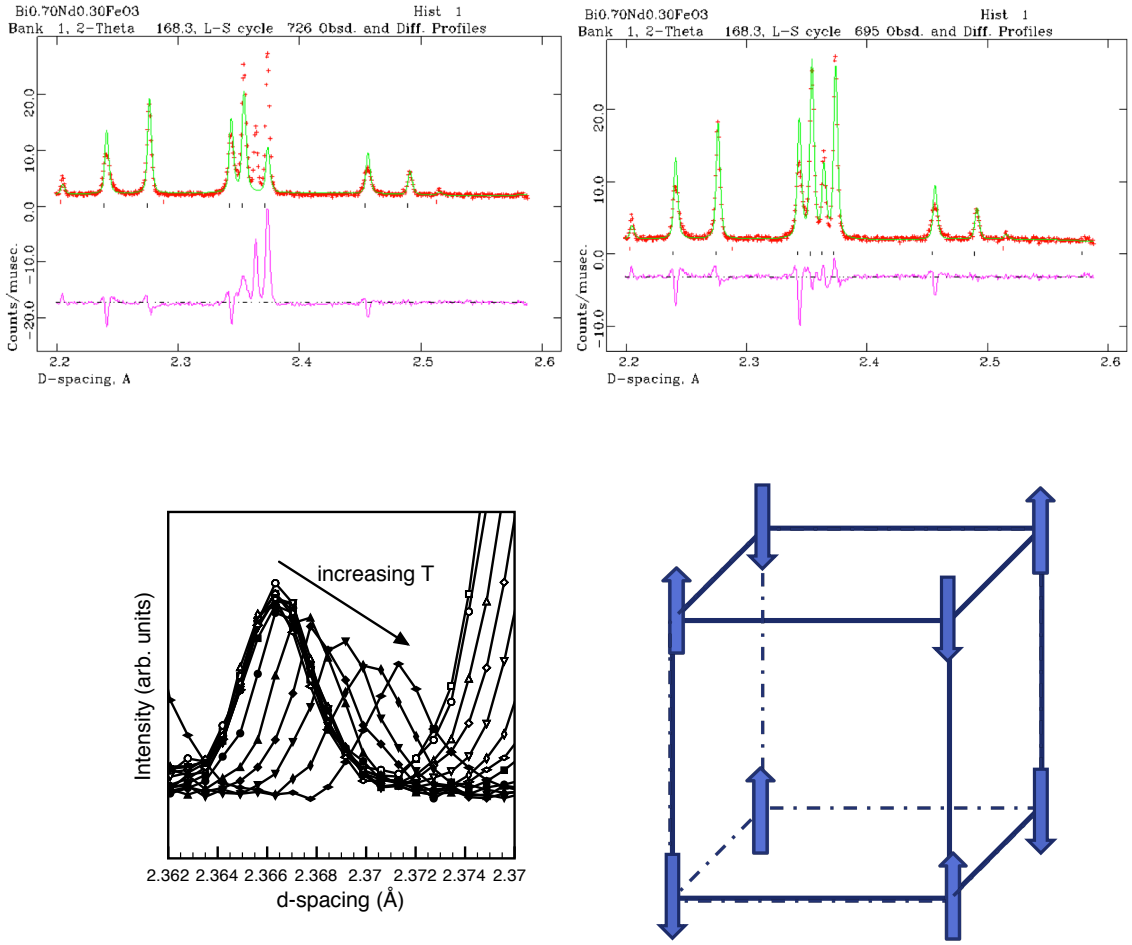

Figure S4: Rietveld refinement profiles of ND data at 50 K without (top left) and with (top right) the magnetic cell included. Note the purely magnetic (130) reflection at 2.36 Å. Temperature dependence of the (130) magnetic reflection (bottom left) over the range 50 to 500 K; representation of G_z type antiferromagnetic ordering (bottom right), where the moments are aligned along the z-axis and arranged in an antiparallel arrangement with respect to nearest neighbours in all three (*x*,*y*,*z*) axes.

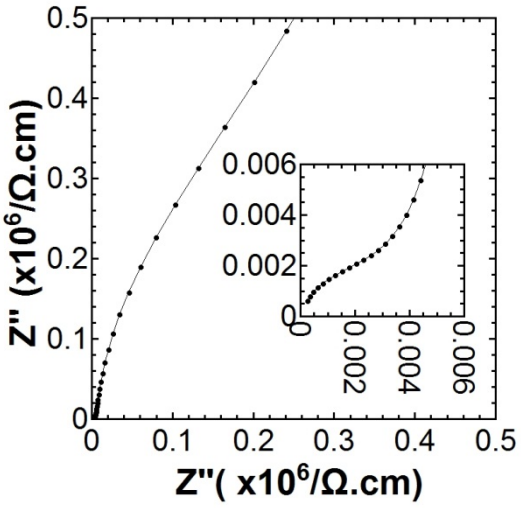

Figure S5: Complex impedance, Z^*, plane plot at 280 K showing the grain boundary and conducting bulk response (inset).

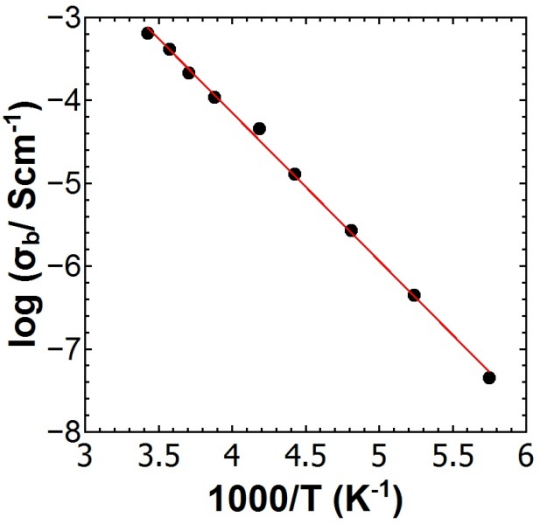

Figure S6: Arrhenius plot of bulk conductivities determined from M^* data; $E_a = 0.35 \pm 0.01$ eV ($R^2 = 0.998$).

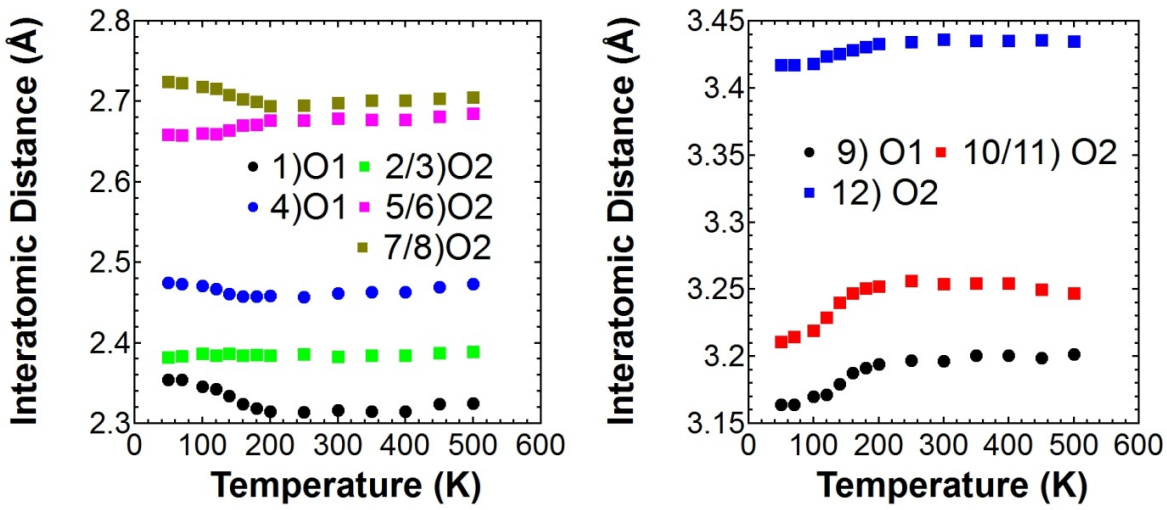

Figure S7: Interatomic distances between the A-site and axial (O1) and equatorial oxygens (O2)

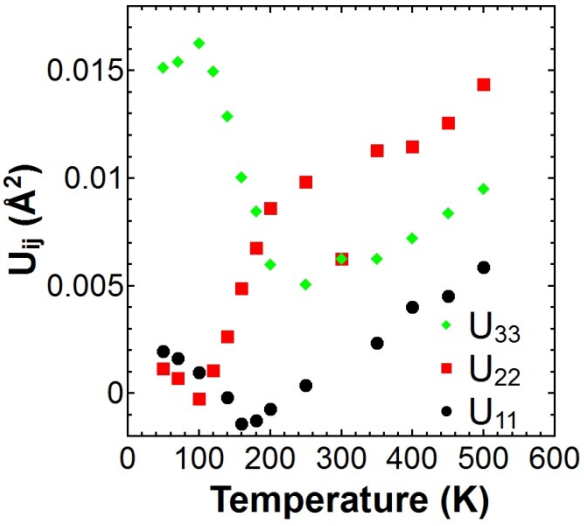

Figure S8: A-site anisotropic atomic displacement parameters (U_{ij}) as a function of temperature along *a* (U_{11}), *b* (U_{22}), and *c* (U_{33}) axes.